

LoRaCompass: Robust Reinforcement Learning to Efficiently Search for a LoRa Tag

Tianlang He, Zhongming Lin, Tianrui Jiang, S.-H. Gary Chan, *Senior Member, IEEE*

arXiv:2511.11190v1 [cs.LG] 14 Nov 2025

Abstract—The Long-Range (LoRa) protocol, known for its extensive range and low power, has increasingly been adopted in tags worn by mentally incapacitated persons (MIPs) and others at risk of going missing. We study the sequential decision-making process for a mobile sensor to locate a periodically broadcasting LoRa tag with the fewest moves (hops) in general, unknown environments, guided by the received signal strength indicator (RSSI). While existing methods leverage reinforcement learning for search, they remain vulnerable to domain shift and signal fluctuation, resulting in cascading decision errors that culminate in substantial localization inaccuracies. To bridge this gap, we propose LoRaCompass, a reinforcement learning model designed to achieve robust and efficient search for a LoRa tag. For exploitation under domain shift and signal fluctuation, LoRaCompass learns a robust spatial representation from RSSI to maximize the probability of moving closer to a tag, via a spatially-aware feature extractor and a policy distillation loss function. It further introduces an exploration function inspired by the upper confidence bound (UCB) that guides the sensor toward the tag with increasing confidence. We have validated LoRaCompass in ground-based and drone-assisted scenarios within diverse unseen environments covering an area of over 80 km². It has demonstrated high success rate (>90%) in locating the tag within 100 m proximity (a 40% improvement over existing methods) and high efficiency with a search path length (in hops) that scales linearly with the initial distance.

Index Terms—Search and Rescue, LoRa Sensing, Localization-based Service, Reinforcement Learning, Contextual MDP

I. INTRODUCTION

The Long Range (LoRa) protocol has long been used for Internet of Things (IoT) communication, known for its wide coverage (1-5km), low power consumption, and low cost [2]. These traits have led to its adoption in IoT tags worn by individuals at risk of going missing, such as mentally incapacitated patients (MIPs—including those with dementia, Down’s syndrome, autism, or psychological disorders), children, and hikers [3]–[8]. Notably, a *LoRa tag* can broadcast signals (on the order of once per minute) over kilometers for months on a single battery. Such longevity and range could provide longer, better safety support for those individuals, superior to other IoT devices like the power-hungry GPS trackers and short-range Bluetooth tags [9]–[12].

When an individual is reported missing, existing approaches to locating the LoRa tag (and thus the individual) uses either a fixed sensor infrastructure or a *mobile sensor* [8], [13], [14]. Since LoRa infrastructure only exists in limited areas, localization based on a mobile sensor has gained increasing traction.

T. He, Z. Lin, T. Jiang, and S.-H. G. Chan are with the Department of Computer Science and Engineering, The Hong Kong University of Science and Technology, Hong Kong (e-mail: {theaf, zmkust, tjiangag, gchan}@cse.ust.hk; corresponding author: Tianlang He.)

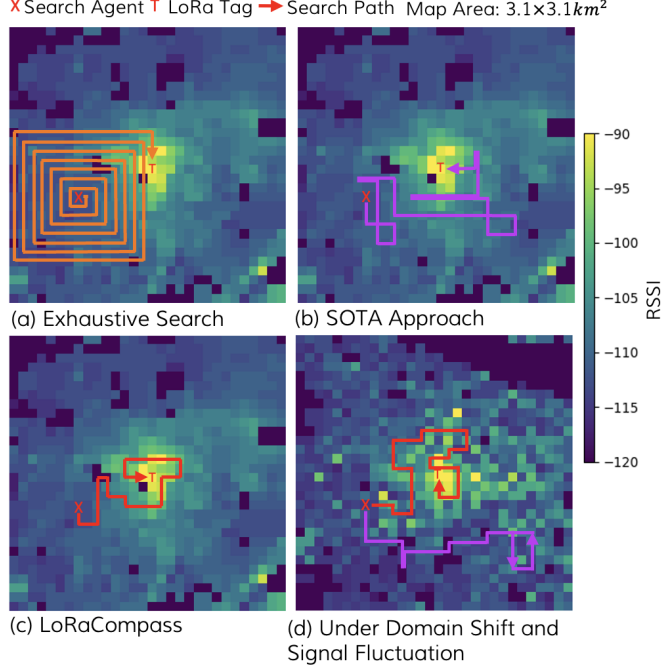


Fig. 1. Search path from an agent at initial location X to a LoRa tag at T , with the RSSI heatmap shown as background. (a) Traditional exhaustive search, which is independent of RSSI, resulting in an inefficient path. (b) State-of-the-art (SOTA) approach [1], achieving a shorter path under the same RSSI heatmap. (c) Our LoRaCompass, demonstrating a more efficient (shorter) search path for the same heatmap. (d) Search path under domain shift and signal fluctuation. The SOTA approach (purple line) fails to converge to the tag owing to path looping, whereas LoRaCompass (red line) remains efficient and robust, successfully converging to the tag.

In a mobile paradigm, a mobile *agent* (e.g., a policeman, caregiver, vehicle, or drone) carries a LoRa sensor and moves sequentially toward the tag, guided by the received signal strength indicator (RSSI) at the sensor.¹ The agent searches for the location with the maximal RSSI, where the tag is normally located.

We divide the search area into a set of regular *grids*, where the grid size corresponds to the distance an agent can travel during the tag broadcast interval.² The agent movement to a neighboring grid point is defined as a “hop,” while an *action* refers to the chosen direction of a hop. A complete search process for a tag follows a repeated cycle: (1) the agent waits and records the RSSI reading at its current grid point; (2)

¹Note that we forgo other signal modalities due to their limited data accessibility and reliance on line-of-sight conditions [14], [15].

²For example, if an agent moves at a speed of 50 meters per minute, and the tag broadcasts every 2 minutes, the grid size is 100 meters.

it transmits the RSSI and its grid location to a server; (3) it receives from the server the *decision* of action for the next grid point; (4) it hops to the designated grid point, and the cycle repeats from step (1). In this paper, we study the important problem in step (3), namely, the sequential decision-making process for an agent to locate a LoRa tag (with the fewest hops) in general environments.

This research problem boils down to two critical questions: **What RSSI feature provides a robust representation for tag directions (relative to agent location) when the search is in a general, unknown environment?** and **How can we design an effective strategy to acquire such a feature in a sequential, dynamic process?** The challenges of addressing these two questions arise from signal fluctuation and domain shift, inherent in the wide-coverage nature of LoRa. Due to long-range propagation, LoRa signals are more prone to dynamic factors (like multipath fading and ambient noise) than short-range signals (e.g., Wi-Fi and Bluetooth), resulting in substantial random RSSI fluctuations. Consequently, an increased RSSI does not necessarily indicate proximity, nor does a decrease signify distance; this makes it challenging to design a robust action representation. Furthermore, the large coverage area introduces systematic shifts in RSSI distribution caused by environmental factors like buildings, vegetation, and terrain. Due to such domain shift, even if we leverage data-driven methods to learn a deep feature of actions from one site, the feature may fail unpredictably at another.

To our knowledge, these two questions remain unanswered in the literature. Prior research on searching for short-range wireless devices often assumes a known RSSI model and thus cannot generalize to LoRa scenarios [16]–[19]. State-of-the-art (SOTA) approaches adopt a purely data-driven methodology, leveraging reinforcement learning (RL) to learn a mapping from RSSI time series to actions in a given site [1], [20]–[22]. However, this method is vulnerable to domain shift and signal fluctuation in practical, unseen scenarios, causing decision errors to propagate throughout the action sequence, culminating in large localization errors. While the field of robust RL provides frameworks to address uncertainty, they often require demanding data collection or highly controllable environments [23], [24]. Such requirements are prohibitively costly, if not impossible, to meet in our problem context.

We observed that the spatial variation of RSSI within a large receptive field provides a robust representation for tag directions. In contrast to noisy RSSI structure on a local scale, the macroscopic, global perspective (e.g., over 20×20 grids) reveals a clear pattern: grid points closer to the tag tend to yield higher RSSI readings (see examples in Figure 1 and Appendix A). This pattern sheds lights on the tag direction despite noise, domain shift, and other environmental factors, as it stems from the physical principle of signal attenuation. We therefore answer the above two questions as follows: **First, a sufficiently large receptive field with full spatial visibility (i.e., ample RSSI samples) provides a robust representation for tag directions in the wild. Second, we can acquire this feature by maximizing the field's visibility during decision-making.**

We propose *LoRaCompass*, a novel, deployable reinforce-

ment learning model for efficient and robust LoRa tag search under domain shift and signal fluctuation. Given a time series of RSSI readings collected on the fly, LoRaCompass maximizes the probability of hopping closer to a tag (exploitation) while simultaneously maximizing the spatial visibility of RSSI (exploration). LoRaCompass determines actions by integrating these two components, enabling the search agent to approach a LoRa tag with increasing confidence as visibility grows. This goal is achieved through two innovative modules, as follows:

- *Robust exploitation model for estimating the action distribution of hop-closer probability:* This model estimates the probability distribution of actions that lead the agent to hop closer to a tag. It is built upon a deep learning architecture designed for robustness. To counter domain shift, its input comes from a novel feature extractor that captures global and local spatial variation of RSSI within a large receptive field. To ensure search efficiency amidst signal fluctuation, the model is trained using a policy distillation loss function.
- *Effective exploration function for computing the confidence gain of actions:* To maximize receptive field visibility, we design a closed-form exploration function inspired by the Upper Confidence Bound (UCB) [25]. This function quantifies the potential confidence gain of each action based on current visibility, thereby mitigating myopic behaviors such as premature convergence and looping that cause large localization errors. Furthermore, it adaptively balances the trade-off between exploitation and exploration in the search process, which optimizes the overall search efficiency.

Having laid methodological foundations, we showcase the robustness and efficiency of LoRaCompass in Figure 1, where a LoRa tag is placed at the center of an urban region (labeled as T) with the underlying RSSI heatmap shown in the background. Starting from its initial location X , an agent must determine its next hop toward T , from four possible actions (directions), based on the RSSI sampled at its current grid point. A traditional exhaustive blanket search strategy is depicted in Figure 1(a), where the agent follows a fixed “spiral” trajectory that is independent of the received signal to cover the entire area. This approach is inefficient, incurring a search cost of $O(s^2)$ hops, where s is the distance between the tag and the agent’s initial location. In contrast, Figure 1(b) shows a much shorter path produced by a SOTA RL approach, which optimizes each hop based on the RSSI sampled at the grid. While SOTA method is efficient in the given scenario, it lacks robustness and often fails to locate the tag under domain shift and signal fluctuation, as illustrated in Figure 1(d) (purple line). By comparison, our LoRaCompass demonstrates both efficiency and robustness in locating the LoRa tag, as illustrated in Figures 1(c) and 1(d) (red line).

Besides the examples above, we have implemented and validated LoRaCompass with extensive experiments of more than 20,000 search processes for both ground-based and drone-assisted scenarios at multiple diverse sites of more than 80km^2 . LoRaCompass, trained merely on any one site, is shown to achieve impressive success rate on other unseen sites (over 90% of the time locating the tag in less than 100m proximity), outperforming SOTA approaches significantly by 40%. It also

TABLE I
SUMMARY OF MAJOR SYMBOLS.

Notation	Description
\mathcal{G}	Global 2D coordinate system ($\mathcal{G} = \{(i, j) \mid i, j \in \mathbb{Z}\}$)
K	Total number of steps in a search process
k	Index of a search step ($k = 0, 1, \dots, K - 1$)
c	Grid coordinate of LoRa tag ($c \in \mathcal{G}$)
u_k	Grid coordinate of agent at step k ($u_k \in \mathcal{G}$)
v_k	RSSI observed at u_k given c ($v_k \sim P(v \mid u_k, c)$)
$v(u)$	RSSI observed at u given c ($v(u) = P(v \mid u, c)$)
a	Categorical action variable ($a \in \{N, E, S, W, O\}$)
$\pi_\theta(u_{0:k}, v_{0:k})$	Policy model mapping search data to action at step k ($a_k = \pi_\theta(v_{0:k}, u_{0:k}), \theta \in \Theta$)
s_k	Vector of search state at step k ($s_k = u_k - c$)
\mathcal{G}_c	2D grid plane taking c as origin ($s_n \in \mathcal{G}_c$)
r_k	Reward value at step k ($r_k \in \{+1, -1\}$)

demonstrates high efficiency, as the search path length scales linearly with the initial distance between the tag and agent.

The remainder of this paper is organized as follows. We first define our problem and model training in Section II, and present LoRaCompass design in Section III, including its feature extractor, exploitation model, loss function, and exploration function. We discuss our extensive experimental results in Section IV. We review related work in Section V and conclude in Section VI. In the Appendix, we present visualizations of experimental RSSI heatmaps and the derivation of exploration function.

II. PRELIMINARIES

In this section, we formulate the search problem in Section II-A and discuss details of model training in Section II-B. The major symbols are summarized in Table I.

A. Problem Formulation

We index the grid points in a search area by a global 2D coordinate system, denoted $\mathcal{G} = \{(i, j) \mid i, j \in \mathbb{Z}\}$, where the i -axis extends from west (W) to east (E), and the j -axis extends from south (S) to north (N). In a search of K total steps, an agent (carrying a LoRa sensor) starts at an initial location $u_0 \in \mathcal{G}$ and searches for a largely immobile LoRa tag at an unknown location $c \in \mathcal{G}$. At step $k = 0, 1, \dots, K - 1$, the agent at location $u_k \in \mathcal{G}$ receives an RSSI observation $v_k \in \{-120, -110, \dots, -30\}$.³ Then, a non-Markovian policy model π_θ (parameterized by $\theta \in \Theta$) uses the history of locations and RSSI observations (or simply, the search history) to determine the agent's action at this step:

$$a_k = \pi_\theta(u_{0:k}, v_{0:k}), \quad (1)$$

where $a_k \in \{N, E, S, W, O\}$ is a categorical variable and O denotes “stop”. The objective of the policy is to guide the agent to the tag location c with the fewest hops and then issue the stop action.

Contextual POMDP: This search problem is fundamentally a contextual partially observable Markov decision process (CPOMDP) [21], [26]. The context is determined by the tag

location c , since it defines the search context (e.g., the building layout in the search area); while the context is unobservable to the policy model. We formulate the search problem as a CPOMDP by defining the eight core elements, as follows:

- **State space:** The search state at step k is a vector from the agent to the tag, denoted $s_k = u_k - c$. The state space is a grid plane taking c as origin, denoted as \mathcal{G}_c .
- **Observation space:** Since states are unknown, we need to observe RSSI from the states for search. The search process is hence partially observable, and the observation space is $[-120, -30] \cap \mathbb{Z}$.
- **Action space:** $\mathcal{A} = \{N, E, S, W, O\}$, as mentioned earlier.
- **Observation function:** The observation function defines the probability of receiving an RSSI observation v_k given the agent location u_k and the underlying (unknown) tag location c . Due to signal noise, we model the observation as a random variable drawn from a distribution determined by u_k and c (as well as the environments in between), expressed as

$$v_k \sim P(v \mid u_k, c). \quad (2)$$

Here, $P(\cdot \mid u_k, c)$ is the RSSI distribution determined by the tag and agent location. Due to domain shift, RSSI distribution of an entire search process varies with the context, i.e., tag location c . The problem is hence CPOMDP.

- **Transition function:** The search state evolves as $s_{k+1} = s_k + \Delta(a_k)$, where $\Delta(a_k)$ is the displacement vector corresponding to action a_k . Since agent may not comply with the instruction in practice, we introduce stochasticity into the transition:

$$a_k = \begin{cases} \pi_\theta(u_{0:k}, v_{0:k}), & \text{with prob } \tau, \\ \mathcal{U}(\mathcal{A}), & \text{with prob } 1 - \tau, \end{cases} \quad (3)$$

with $\tau \in [0, 1]$ as a compliance threshold. Empirical study of the effect of τ is shown in Figure 12.

- **Reward function (available only during training):** The reward function encourages actions that move the agent closer to the tag and penalizes otherwise. It is formally defined as:

$$R(s_{k+1} \mid s_k) = \begin{cases} +1, & \|s_{k+1}\| < \|s_k\| \text{ or } \|s_{k+1}\| = 0, \\ -1, & \text{otherwise,} \end{cases}$$

where the reward at step k is $r_k = R(s_{k+1} \mid s_k)$. Note that this reward signal is exclusively available during the training phase; the deployed policy must operate without it during real-world testing.

- **Initial state distribution:** We consider a general setting where the initial search state s_0 is uniformly distributed over the state space \mathcal{G}_c , i.e., $s_0 \sim \mathcal{U}(\mathcal{G}_c)$.
- **Context distribution:** The context, determined by the tag location c , is modeled as a random variable uniformly distributed over the grid, i.e., $c \sim \mathcal{U}(\mathcal{G})$.

Problem Statement: Our goal is to locate a LoRa tag in an unknown environment with the fewest hops. This translates to learning a policy π_θ that maximizes the expected cumulative reward in the CPOMDP, i.e.,

$$\max_{\theta \in \Theta} \mathbb{E}_{c \sim \mathcal{U}(\mathcal{G})} \left[\sum_{k=0}^{K-1} r_k^{(\pi_\theta, c)} \right], \quad (4)$$

³In our experiments, signal loss is imputed as -120 dBm.

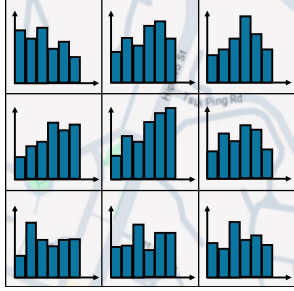


Fig. 2. Illustration of our realistic simulator used for on-policy training. The observation function is simulated by RSSI histograms collected from each grid point.

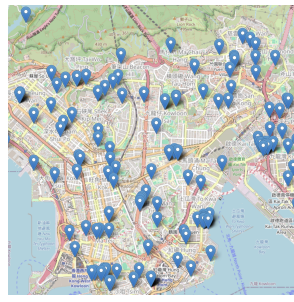


Fig. 3. Distribution of LoRa gateway in an urban region of 40km². Gateways are marked by blue labels.

where $r_k^{(\pi_\theta, c)}$ is the reward received at step k when searching for a tag at c . Obviously, a policy model cannot be trained on all possible tag locations. It must instead learn from the search for one or more tag locations (i.e., $\{c\} \subset \mathcal{G}$) and generalize to the search for any other tag locations (i.e., $\forall c \in \mathcal{G}$).

B. On-Policy Model Training

The trial-and-error nature of reinforcement learning is prohibitively costly for training, which is especially nontrivial for a problem to be deployed in real-world environments. Therefore, we adopt a deployable paradigm: the policy is learned in a realistic simulator and directly deployed for real-world operations (without any retraining). Central to a realistic simulator is to mirror the real observation function. To achieve this, our training process has two stages: data collection and simulation. In data collection stage, we fix a tag location and collect RSSI distributions from the grid points around the tag. The collected data simulate the observation function for the search of one tag location, as illustrated in Figure 2. In the simulation stage, we develop a simulator powered by the collected data to conduct on-policy training. The simulator for the search of one tag location is thus defined as “one site”.

This training approach is both effective and feasible, while the training cost can be further reduced by data crowdsourcing. As shown in Figure 3, existing LoRa infrastructure in cities allows data collection from volunteers (e.g., caregivers, bus drivers, and postworkers) wearing LoRa tags and GPS devices [13], [27], [28].⁴ Last but not the least, our policy model, i.e., LoRaCompass, is context-efficient: it merely requires one training site and can generalize to other unseen sites, owing to its design embedded with domain knowledge (which is validated in Section IV).

III. LORACOMPASS DESIGN

In this section, we present the design of LoRaCompass. We begin by an overview in Section III-A, and discuss the feature extractor in Section III-B. Then, we delineate the exploitation model with its loss function in Sections III-C and III-D, respectively. Finally, we present the exploration function in Section III-E.

⁴The observation function can be centered at either sensor or tag.

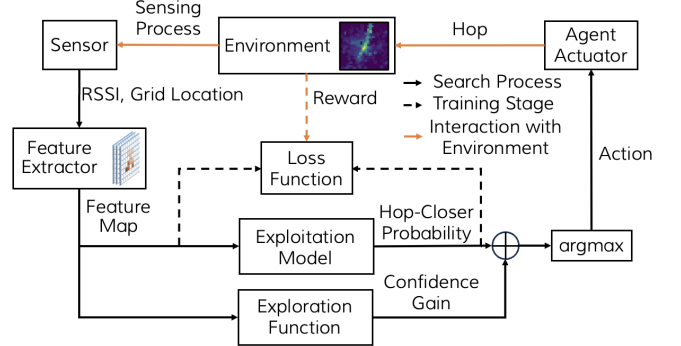


Fig. 4. System diagram of LoRaCompass.

A. System Overview

The system diagram of LoRaCompass is shown in Figure 4. It interacts with the environment via a LoRa sensor (integrated with a location tracker) and an agent actuator (e.g., the flight control of an UAV). The environment is defined by CPOMDP framework in Section 4, including the observation function in Eq. (2), reward function in Eq. (4), etc.

As specified in Eq. (1), LoRaCompass takes the search history $(u_{0:k}, v_{0:k})$ as input and outputs actions (a_k) for the actuator to execute the next hop. To tackle domain shift, LoRaCompass first constructs a *feature map* from the search history using a feature extractor. This process is shown as

$$\{u_{0:k}, v_{0:k}\} \mapsto \mathcal{M}_k, \quad (5)$$

where \mathcal{M}_k is the feature map at step k . This feature map allows to capture global and local RSSI spatial feature from a large receptive field, which provides a robust representation of tag direction relative to agent location. Based on the feature map, an exploitation model f_θ estimates the action distribution of hop-closer probability:

$$\pi_e(a | \mathcal{M}_k) = f_\theta(\mathcal{M}_k). \quad (6)$$

In the training stage, the exploitation model learns from a loss function based on policy distillation to boost search efficiency amid signal fluctuation.

On the other hand, we design an exploration function, denoted by g , to optimize RSSI visibility on the feature map, ensuring LoRaCompass to effectively acquire more robust feature as visibility grows. It models the visibility as decision confidence and estimates the confidence gain of each action given current visibility. LoRaCompass finally determines an action to maximize the combined objective:

$$a_k = \arg \max_{a \in \mathcal{A}} [\pi_e(a | \mathcal{M}_k) + g(a, \mathcal{M}_k)]. \quad (7)$$

The following subsections detail the design of these modules.

B. Feature Extractor

Given search history $(\{u_{0:n}, v_{0:n}\})$, we study extracting a RSSI feature that provides a robust representation of tag direction relative to the agent location under domain shift and signal fluctuation. Our observation is shown in Figure 5. While

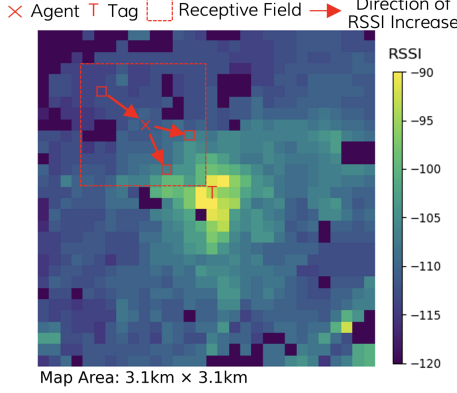


Fig. 5. Observation behind feature extraction: Within a sufficiently large receptive field (centered at the agent location), the RSSI tends to be higher closer to the tag, and lower further away from it. This pattern sheds light on tag direction independent of domain shift and signal fluctuation.

RSSI on a local scale is often noisy, it shows a clear pattern that RSSI is higher closer to the tag, and lower further away from it, given a sufficiently large receptive field (centered at the agent location). This pattern sheds light on the tag direction, which is due to signal attenuation; i.e., the signal strength always decreases with travel distance due to energy expenditure. This physical principle is independent of domain shift and noise. Though we cannot change the search history at this stage, we can present the time series of RSSI into a better map representation to reflect this pattern. It provides a robustness basis that higher visibility on the map leads to more robust representation of tag directions. To implement this idea, we build a feature extractor to capture the RSSI spatial variation and visibility.

First, we capture the RSSI spatial distribution within a large receptive field. Let $v(u)$ denote an RSSI sampled at u , and $\bar{v}(u)$ denote the mean of all RSSI samples collected at this grid point (i.e., $\forall v(u) \in v_{0:k}$). Rewriting agent location at step k as $u_k = (i_k, j_k)$, we build a signal map by

$$\mathcal{M}_k^{(s)} = \{\bar{v}(i, j) \mid |i - i_k|, |j - j_k| \leq m\}, \quad (8)$$

where $m = 1, 2, \dots$ controls the map size (parameter study is in Figure 15). Then, we capture the RSSI spatial variation relative to the agent location by a variation map, defined as

$$\mathcal{M}_k^{(v)} = \left\{ v - \bar{v}(i_k, j_k) \mid v \in \mathcal{M}_k^{(s)} \right\}. \quad (9)$$

Note that $\mathcal{M}^{(v)}$ presents RSSI spatial variations more straightforwardly than $\mathcal{M}^{(s)}$. It hence provides better representation for tag directions (see ablation study in Figure 14). Yet, the signal map is important for tackling signal fluctuation and balancing the exploitation and exploration.

On the other hand, we define the visibility on a grid point as the number of agent visits at the point. Let $\#(u, U)$ denote the frequency of element u appearing in a set U . The visibility within the receptive field, i.e., the visibility map, is defined as

$$\mathcal{M}_n^{(b)} = \{\#((i, j), u_{0:k}) \mid |i - i_k|, |j - j_k| \leq m\}. \quad (10)$$

Here, we implement a trick: we binarize the visibility map into visited and unvisited states when estimating actions, which

reduces the randomness from the visit counts; while the visit numbers are important for exploration, which will be covered later.

Finally, the three feature maps constitutes a feature map, shown as

$$\mathcal{M}_k = \left[\mathcal{M}_k^{(s)}, \mathcal{M}_k^{(v)}, \mathcal{M}_k^{(b)} \right], \quad (11)$$

with $[\cdot]$ denoting the concatenation operation.

C. Exploitation Model

Our ultimate goal is to estimate the action to hop closer to the tag. Based on the feature map, we build an exploitation model to estimate action distribution of hop-closer probability. It is based on deep learning architecture designed for robustness against signal fluctuation.

First, we use a convolutional neural network (CNN) to aggregate the feature map into a search feature, given as

$$z_k = f_{\theta_1}(\mathcal{M}_k), \quad (12)$$

where z_k is the search feature at step k . The search feature is designed to be robust against signal fluctuation, owing to our loss function (to be presented in the next section). Then, we employ a multilayer perceptron (MLP) with a Softmax function, mapping search feature to a probability distribution of actions, shown as

$$\pi_e(a_k \mid \mathcal{M}_k) = f_{\theta_2}(z_k), \quad (13)$$

where $\theta = [\theta_1, \theta_2]$. Note that our design adheres to the convention for processing map data, and other model structures may also be applicable [21], [29]–[31].

The exploitation model learns an important piece of human knowledge: a preference to pursue grid points with higher RSSI. This knowledge arises from the feature map, which provides a strong correlation between the tag directions and the directions or RSSI increase. Such a preference largely prevents the search from path divergence, especially when the visibility of feature map is high. Also, as it is embedded with the human knowledge, the exploitation model does not need to learn it from massive training data. The exploitation model is hence context-efficient, which requires merely one site for training and can generalize to other unseen ones (see Tables II and III).

D. Loss Function for Exploitation

In this section, we present the loss function to train the exploitation model. Through the loss function, we aims to (1) maximize the probability of actions to hop closer to a tag, (2) minimize the search inefficiencies caused by signal fluctuations, and (3) enable an efficient training process with the fewest epochs. Correspondingly, the overall loss function has three parts, as follows:

$$L(\theta) = L_{PG}(\theta) + \omega_1 L_{PD}(\theta_1) + \omega_2 L_{SL}(\theta_1), \quad (14)$$

where ω_1, ω_2 are the weights for their relative importance.

Policy gradient (PG) loss function to maximize hop-closer probability: Policy gradient is a classic method to optimize

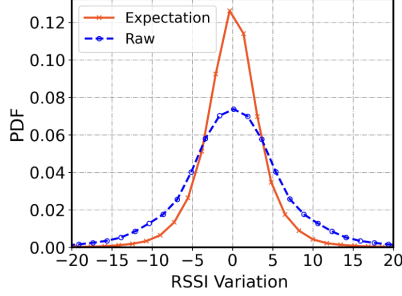


Fig. 6. Probability distribution (PDF) of RSSI variation between straight-neighboring grids.

policy-based RL. Recall that r_k is the reward value at step k . Our PG loss function is presented as

$$L_{PG}(\theta) = -\mathbb{E}_{a_k \sim f_\theta} \left[\sum_{k=0}^{K-1} r_k \log \pi_e(a_k \mid \mathcal{M}_k) \right], \quad (15)$$

recall that $\pi_e(a_k \mid \mathcal{M}_k)$ is the exploitation model output. We adopt policy gradient for convenience, as the reward function can be directly used as the advantage function [21], [32].

Policy distillation (PD) to mitigate signal fluctuation: Due to signal fluctuation, an agent often needs to visit to a grid point multiple times for high visibility, thus leading to search inefficiency. We aim to design a loss function to reduce the number of visits. Our intuition is to leverage the conditional expectation of RSSI across locations, expressed as

$$\mathbb{E}[v(u) \mid u_{0:k}, v_{0:k}]. \quad (16)$$

If RSSI samples at one grid point can estimate the expectation at another, visit counts can be reduced. Here, since the signal map is unpredictable due to domain shift, we focus on the visited grids, i.e., $u \in u_{0:n}$.

We implement this idea using policy distillation [33]. We train two agents in parallel: the student agent in a fluctuation-based simulator and the teacher agent in a fluctuation-free mode.⁵ By minimizing decision differences, the student agent learns to counter signal fluctuation. To synchronize search history, we directly enforce this constraint on the search feature z_k (from Eq. (12)). The policy distillation loss function of a complete search process is given as

$$L_{PD}(\theta_1) = \sum_{k=0}^{K-1} \text{MSE}(z_k, z'_k), \quad (17)$$

where z'_k is the search feature of the teacher agent, and MSE calculates the mean squared error. The PD loss function enables the efficient search amid signal fluctuation, which is validated in Figure 19.

Theoretically, the PD loss function is effective because it reduces the bias in the second moment on the signal map ($\mathcal{M}^{(s)}$). The bias is due to signal fluctuation, as it inflates the variance of observed RSSI differences relative to the difference of their expectations:

$$\mathbb{E}[|\bar{v}(u_p) - \bar{v}(u_q)|] > |\mathbb{E}[v(u_p)] - \mathbb{E}[v(u_q)]|, \quad (18)$$

⁵They are two modes provided by our simulator.

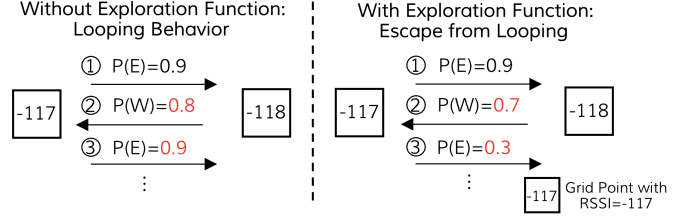


Fig. 7. Exploration function facilitates escaping from path divergence (right-hand side).

where $u_p, u_q \in u_{0:k}$ and $u_p \neq u_q$. Figure 6 further illustrates the bias between straight-neighboring grid points to substantiate this explanation. By minimizing the PD loss, we enforce visited points to act as mutual conditional expectations to reduce this bias, thus improving efficiency under fluctuation.

Supervised learning (SL) to accelerate training process: We additionally introduce a trick to reduce the number of training epochs based on supervised learning. While supervised learning does not capture the stochastic nature of the search problem [34], it can quickly embed prior knowledge into the search feature, hence accelerating the training convergence. By implementing this idea, we propose a SL loss function, shown as

$$L_{SL}(\theta_1) = \sum_{k=0}^{K-1} |(P(a_k \mid z_k) - P(a_k \mid s_k)|, \quad (19)$$

where we use a linear regression from z_k to a . Here, the discrepancy of the probability distribution is short for

$$\begin{aligned} & |P(a_k \mid z_k) - P(a_k \mid s_k)| \\ &= \sum_{a \in \mathcal{A}} |P(a \mid z_k) - P(a \mid s_k)|. \end{aligned} \quad (20)$$

We validate in Figure 20 that SL loss function can improve training efficiency by a large margin.

E. Exploration Function

In this section, we present our exploration function for maximizing the feature map visibility. Without it, the policy degenerates to greedy action selection ($\arg \max_{a \in \mathcal{A}} \pi_e(a \mid \mathcal{M}_k)$), which is prone to large localization errors. The root cause is path looping: initially low map visibility creates high uncertainty in the action probabilities $\pi_e(a \mid \mathcal{M}_k)$. This uncertainty can trap the agent in a path loop. A concrete example is illustrated on the left of Figure 7, where an agent oscillates between two neighboring grid points. When at the western grid, high uncertainty leads it to favor an 'E' hop; when at the eastern grid, it rather favors a 'W' hop. The longer the loop continues, the less likely it is to escape (due to decreasing feature map variations), culminating in large localization errors.

Loops can be complex and unpredictable, involving any number of grids or even nested structures.⁶ While introducing randomness can facilitate escape [21], [35], it merely mitigates rather than avoids looping, often at the expense

⁶The loop involving only one grid point outside the tag proximity is called premature convergence.

of search efficiency (see Figure 18). We posit that looping occurs because the uncertainty in probability estimates fails to decrease over time. To escape loops, a selected action should not only maximize the immediate hop-closer probability but also minimizes the uncertainty for future decisions. This goal of foresight is written as

$$\arg \max_{a_k \in \mathcal{A}} \left[\pi_e(a_k | \mathcal{M}_k) - \beta_k |\pi_e(a_{k+1} | \mathcal{M}_{k+1}) - \pi_e(a_{k+1} | \mathbb{E}(\mathcal{M}_{k+1}))| \right], \quad (21)$$

where the calculation of $|\cdot|$ follows Eq. (20), and β_k is the importance weight of exploration at step k . We identify that the decision uncertainty primarily stems from an incomplete feature map (detailed explanation is in Appendix). Therefore, the future decision uncertainty (the second term) is the discrepancy of probability estimates from the anticipated feature map (\mathcal{M}_{k+1}) and its ideal, fully-visible counterpart ($\mathbb{E}(\mathcal{M}_{k+1})$).

While directly computing this uncertainty term remains impractical, we draw inspiration from the Upper Confidence Bound (UCB) to design an exploration function that effectively estimates it. The function quantifies the confidence gain of an action and uses it to adaptively balance exploitation and exploration, shown as

$$\begin{aligned} g(a, \mathcal{M}_k) &= \beta \frac{e^{\alpha \Delta v_k} - 1}{e^{\alpha \Delta v_k} + 1} \left(\frac{1}{\sqrt{n_a}} - \frac{1}{\sqrt{n_a + 1}} \right) \\ &\approx \beta_k \left(|\pi_e(a_k | \mathcal{M}_k) - \pi_e(a_k | \mathbb{E}(\mathcal{M}_k))| \right. \\ &\quad \left. - |\pi_e(a_{k+1} | \mathcal{M}_{k+1}) - \pi_e(a_{k+1} | \mathbb{E}(\mathcal{M}_{k+1}))| \right). \end{aligned} \quad (22)$$

We show a detailed derivation of the exploration function in Appendix, and provide an intuitive explanation of how the exploration function prevents looping behaviors as follows:

- Estimating Confidence Gain: Instead of directly estimating the decision uncertainty, the function estimates the confidence gain of an action. This is an efficient way to operationalize the objective in Eq. (21). Since the current uncertainty is fixed, maximizing confidence gain is equivalent to minimizing future uncertainty.
- $1/\sqrt{n_a} - 1/\sqrt{n_a + 1}$: This term estimates the confidence gain for action a , where $n_a \in \mathbb{Z}^+$ counts the visits at next agent location if action a is executed. After applying this term, an agent in a loop will experience decreasing confidence gain for the looping actions, consequently promoting escape. In the right-hand side of Figure 7, we show an example that this term enables loop escaping (decisions are presented in probability).
- $\beta(e^{\alpha \Delta v_k} - 1)/(e^{\alpha \Delta v_k} + 1)$: This term automatically balances between exploitation and exploration. Here, Δv_k is the difference of current RSSI observation v_k to a reference measured at the tag location (\bar{v}_c):

$$\Delta v_k = \bar{v}(c) - v_k. \quad (23)$$

When the agent receives a v_k that is very close to the reference, this term will reduce the weight for exploration and let the exploitation model to decide whether to stop or not. This allows the search to efficiently land a convergence

once the tag is found. Additionally, α is a proximity variable tuning the convergence behavior (see Figure 17); β is a general weight for the exploration behavior (see Figure 16).

In summary, our LoRaCompass redesigns exploitation and exploration in terms of the feature extractor, exploitation model, loss function for exploitation, and exploration function. All designs are tailored to LoRa tag search, enabling its robustness and efficiency under domain shift and signal fluctuation to support practical deployment.

IV. ILLUSTRATIVE EXPERIMENTAL RESULTS

In this section, we show empirical results to validate LoRaCompass. We introduce the experimental setting in Section IV-A, and discuss illustrative results in Section IV-B.

A. Experimental Setting

We have validated LoRaCompass through extensive experiments in real-data experiments and real-world deployment. We conduct real-data experiments to train and study its performance, and then implemented it in our existing search system in both ground-based and drone-assisted scenarios to demonstrate its real-world deployability.

Our real-data experiment is based on the simulator in Section II-B. The data are collected from five $4 \times 4 \text{ km}^2$ sites located in diverse urban and suburban environments (including various unpredictably diverse environmental factors like houses, parks, streets, etc.), built on vehicle-based crowdsourcing provided by [27]. The five sites totally contain 345,700 RSSI samples, and their RSSI heatmaps are shown in Appendix A. We train LoRaCompass on any one of the sites and test it on others (thus, all testing sites are unseen to the model). Our experiment at each site includes extensive search processes, whether in training or testing. In each search, the agent starts at a (uniformly) random distance to the tag, ranging from 200m to 2,500m, dubbed as *initial distance* (i.e., $\|s_0\|_2$). In total, our experiment includes more than 20,000 search processes in testing at various initial distances in the heterogeneous five sites.

Our existing search system is shown in Figure 8. In actual deployment, the individual will carry a lightweight, portable LoRa tag (Figure 8c), which emits signals approximately once per minute and has a battery life of over one year without recharging. When a missing person is reported, the alert will be disseminated through the platform, activating volunteers to search for the tag. In drone-assisted searches, a drone equipped with a LoRa sensor (Figure 8b) will listen for tag signals. Upon receiving each signal, the sensors will report the RSSI and GPS location to our backend system via a 4G network (Figure 8d). The backend, powered by our trained model, will guide either the drone pilot or autopilot software to the next move. Ground searches operate similarly, with a caregiver carrying the LoRa sensor. The ground search of our onsite experiment is conducted in a $4 \times 4 \text{ km}^2$ residential area, including residential blocks, shopping malls, sidewalks, overpasses, and parks. Our drone search is on a university campus with a legal flying permit.

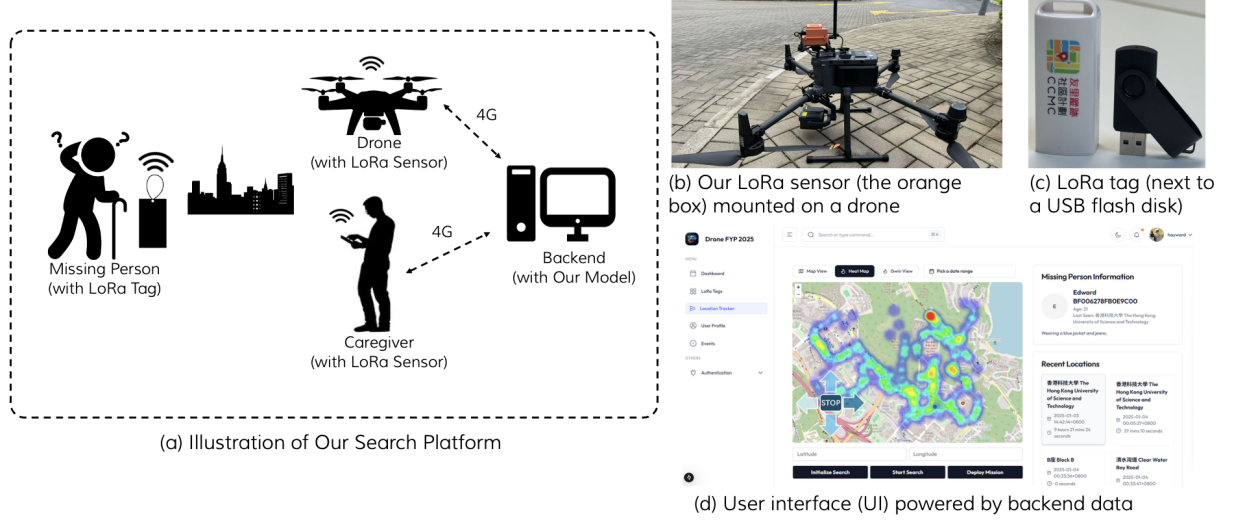


Fig. 8. Illustration of our existing search system (a). In the drone search scenario, a LoRa sensor is mounted on the drone (b) to detect signals from a lightweight IoT tag (c). Upon receiving a signal, the sensor reports its RSSI and GPS location to the backend system via 4G networks (d, showing dummy personal data). The backend server, integrated with our model, guides the drone or ground sensors on their next hops.

We evaluate LoRaCompass in terms of *success rate* and *efficiency*. The success rate is defined as the proportion of searches that converge within a specified proximity threshold d to the target tag. Let $w = 1, 2, \dots, W$ index all independent search processes in evaluation, and $s_{w,k}$ denote the k th state in the w th search process. Success rate is calculated as

$$\text{Success Rate} = \frac{\sum_{w=1}^W \mathbb{1}(\|s_{w,K}\|_2 < d)}{W}, \quad (24)$$

where we set $d = 100\text{m}$ by default. Search efficiency is quantified by the number of steps required to find a tag relative to the shortest path (between 0 and 1). Let k_w^* denote the earliest step before convergence (for staying within the proximity for q hops) in the w th search process, and \mathcal{W} is the set of successful search indexes. Search efficiency is computed as

$$\text{Efficiency} = \frac{1}{|\mathcal{W}|} \sum_{w \in \mathcal{W}} \frac{\|s_{q,0}\|_1}{k_w^*}. \quad (25)$$

For instance, the efficiency of 0.1 means that the search needs 10 times the steps relative to the shortest path length (Efficiency = 1 is theoretically impossible to achieve).

Our baseline approaches are:

- *Ranging method* [20] is the classic method for searching LoRa tag. It leverages RSSI ranging to estimate the tag location, i.e., $\{u_{0:n}, v_{0:n}\} \rightarrow c$, and navigates an agent toward the estimated location.
- *Nelder-Mead simplex algorithm* [19] is a heuristic method for non-derivative trajectory-based optimization. The search decision depends on the simplices sampled in the search.
- *Robins-Monro (RM) algorithm* [18] is an approach for stochastic approximation, which considers momentum to address noisy search. We implement it based on the simplex method.

- *CMIYC (DRL)* [1] is the SOTA reinforcement learning approach designed for LoRa tag search based on LSTM, while it fails to consider domain shift and signal fluctuation.

Unless specified otherwise, we set the grid size as $100 \times 100\text{m}^2$, maximum steps as $K = 500$, and convergence threshold as $q = 4$. The CNN has three layers of 3×3 kernels with padding and stride as 1. The kernel numbers are 16, 32, and 64. The MLP has three layers with feature size as 128. The entire model is optimized by Adam optimizer with learning rate as $1e-3$ and batch size as 50. The initial distances in testing are uniformly distributed, and we repeat each experiment by 10 times.

B. Illustrative Results

Table II reports the success rates of comparative schemes within a 2km initial distance, with models trained on ‘Site 1’ and tested on other sites. The Ranging method fails in most cases due to substantial localization errors. While the RM method surpasses the Simplex method by accounting for signal noise, both lack the flexibility to handle complex observation functions in LoRa scenarios. Although CMIYC leverages DRL to outperform the preceding methods on the training site, its performance is hampered by signal fluctuation and further deteriorates during testing due to sensitivity to domain shift. In contrast, LoRaCompass achieves a high success rate ($>90\%$) across all sites, validating its robustness to both signal fluctuation and domain shift.

Table III shows results consistent with Table II using a different training site. We did not show *RM method* and *Simplex method* since their performance is independent of training. The table demonstrates that LoRaCompass maintains a high success rate, confirming its effectiveness and context-efficiency across varying training environments.

Figure 9 plots success rate against initial distance. LoRaCompass maintains a success rate exceeding 90% until

TABLE II
SUCCESS RATE OF COMPARISON SCHEMES.

	Ranging	Simplex Method	RM Method	CMIYC (DRL)	LoRaCompass
Site 1*	0.042 \pm 0.010	0.235 \pm 0.013	0.502 \pm 0.018	0.683 \pm 0.018	0.996 \pm 0.003
Site 2	0.022 \pm 0.009	0.269 \pm 0.037	0.477 \pm 0.016	0.385 \pm 0.021	0.910 \pm 0.009
Site 3	0.023 \pm 0.005	0.222 \pm 0.005	0.439 \pm 0.026	0.366 \pm 0.015	0.974 \pm 0.006
Site 4	0.029 \pm 0.005	0.314 \pm 0.022	0.55 \pm 0.022	0.375 \pm 0.012	0.946 \pm 0.015
Site 5	0.026 \pm 0.006	0.224 \pm 0.028	0.436 \pm 0.020	0.368 \pm 0.009	0.918 \pm 0.016
Mean	0.027 \pm 0.002	0.253 \pm 0.009	0.479 \pm 0.013	0.373 \pm 0.007	0.940 \pm 0.007

* Training Site

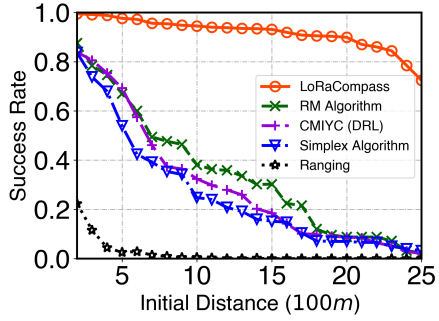


Fig. 9. Success rate versus initial distance.

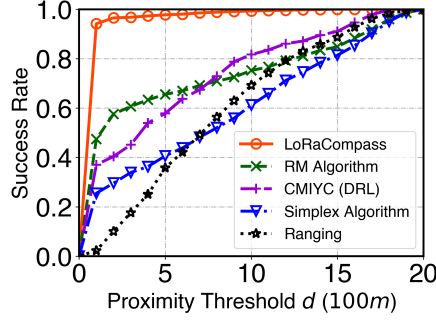


Fig. 10. Success rate versus proximity threshold (localization error).

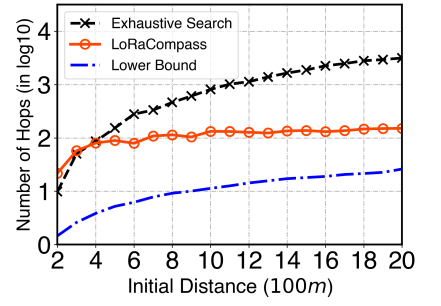


Fig. 11. Number of hops versus initial distance.

TABLE III
SUCCESS RATE BASED ON A DIFFERENT TRAINING SITE.

	Ranging	CMIYC (DRL)	LoRaCompass
Site 2*	0.030 \pm 0.014	0.654 \pm 0.002	0.981 \pm 0.006
Site 1	0.016 \pm 0.006	0.322 \pm 0.008	0.936 \pm 0.006
Site 3	0.029 \pm 0.007	0.346 \pm 0.012	0.960 \pm 0.010
Site 4	0.029 \pm 0.009	0.289 \pm 0.026	0.923 \pm 0.010
Site 5	0.023 \pm 0.007	0.357 \pm 0.008	0.924 \pm 0.009
Mean	0.026 \pm 0.004	0.329 \pm 0.030	0.936 \pm 0.017

* Training Site

the distance reaches 2km. Beyond this range, performance declines due to frequent signal loss, under which the search effectively reduces to a random walk.

Figure 10 shows the success rate against proximity threshold (localization errors). LoRaCompass converges within 100m of the tag in 94% of cases and within 500m in 98% of cases, further validating its practical applicability.

Figure 11 plots convergence steps (on log10 scale) against initial distance, with exhaustive search and shortest path (achievable only with ground truth) as references. The hops of exhaustive search grow quadratically with distance, which is highly inefficient. In contrast, LoRaCompass exhibits a satisfactory, near-linear trend, highlighting its superior efficiency.

Figure 12 demonstrates the robustness of LoRaCompass against random action noise. It maintains a >90% success rate even with 50% compliance on model decisions, owing to the robust exploitation and effective exploration (which considers uncertainty). This result confirms the satisfactory deployability of LoRaCompass in unpredictable environments.

Figure 13 illustrates the collaborative search of LoRaCompass using multiple agents initiating independent paths from the same location. A search is considered successful if any

sensor locates the tag. The results show that both success rate and efficiency improve with the number of sensors, achieving a >98% success rate and a high efficiency score of 0.3 with only three agents. This demonstrates a viable path to significantly enhance search performance through sensor cooperation.

Figure 14 presents an ablation study on the feature maps in Eq. (11). The results indicate that the variation map ($\mathcal{M}^{(v)}$) plays a critical role by capturing spatial RSSI structures; the visibility map ($\mathcal{M}^{(b)}$) provides essential guidance on signal availability; and the signal map ($\mathcal{M}^{(s)}$) is essential for robustness against signal fluctuation. Collectively, all three components are vital for achieving the high success rate.

Figure 15 shows a parameter study on the map size m in Eq. (8). The success rate increases with m and saturates beyond $m = 10$, indicating this size is sufficient for stable performance. Consequently, we set $m = 10$ in our experiments.

Figure 16 shows parameter study of β in exploration function shown in Eq. (22). The success rate increases with β , reaches plateau at $\beta = 8$, and slightly decreases after $\beta = 13$. This is because β controls the weight of the exploration function for loop escaping, while a too large weight may diminish the exploitation. We hence use $\beta = 8$.

Figure 17 shows that proximity parameter α affects both success rate and efficiency (see Eq. (22)). If α is too small, it leads to low success rate due to trapping. If α is too large, the search needs more steps to reach a convergence, resulting in low efficiency. We hence use $\alpha = 0.5$.

Figure 22 compares our exploration function with other common strategies. *Greedy* selects the hop of the highest probability, ϵ -*greedy* is similar to Eq. (3), and *Sampling* picks on the hop probability. In the figure, *Greedy* shows low success rate caused by trapping, yet its high efficiency is only

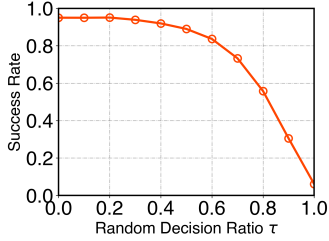


Fig. 12. Success rate versus decision randomness.

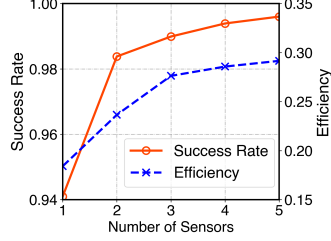


Fig. 13. Case Study: multi-sensor (multi-agent) scenarios.

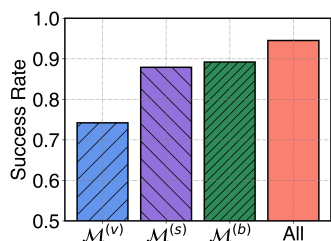


Fig. 14. Ablation study: search map.

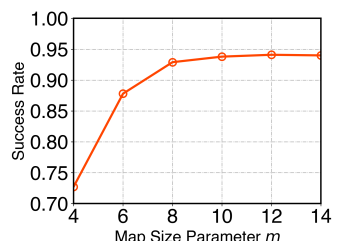


Fig. 15. Parameter study: map size.

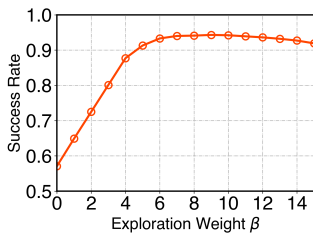


Fig. 16. Parameter study: exploration weight.

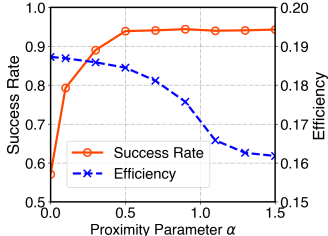


Fig. 17. Parameter study: proximity parameter.

for a few successful cases. *ε-greedy* and *Sampling* introduce randomness to alleviate the looping issue; however, their methods trade off efficiency. In comparison, our exploration function achieves both high success rate and efficiency, owing to its consideration for decision uncertainty.

Figure 19 shows the parameter study of policy distillation in Eq. (14). In the figure, search efficiency increases with its weight (ω_1) since it mitigates signal fluctuation. In the experiment, we use $\omega_1 = 1.5$.

In Figure 20, we study training efficiency with $\omega_2 = 1$. In the figure, policy gradient (PG) achieves higher success rate than supervised learning (SL), but PG converges more slowly than SL. Our trick to combine them, shown by PG+SL, achieves both effectiveness and efficiency.

Figure 21 shows LoRaCompass performance in our on-site experiment. Our model can be directly extended to real-world deployment owing to its robust feature extractor, loss function, and exploration design. Note that the drone search outperforms ground scenario due to the milder multipath fading and loss rate. Also, drone search can better comply with policy model with fewer map constraints.

Finally, we show in Figure 22 a trajectory of ground search. The agent starts from X to search for the tag at T . The agent moves in a normal walking speed, leading to the travel distance of around 100m per hop (marked by the red dots). When restricted by the map, the agent selects the best viable decision from LoRaCompass instructions. In the figure, despite the substantial signal noise and loss rate (more than 10%), LoRaCompass still can navigate the agent to the tag proximity. This has validated the robustness and efficiency of LoRaCompass in practice.

V. RELATED WORK

Existing LoRa tag localization methods operate on either a fixed sensor infrastructure or a mobile sensor paradigm [2],

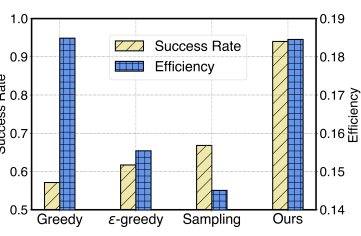


Fig. 18. Comparison of exploration strategies.

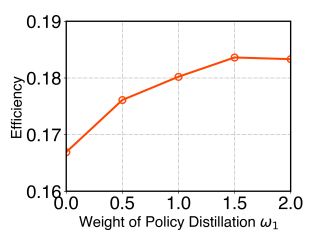


Fig. 19. Parameter study: policy distillation.

[13], [27], [28]. Between them, the mobile approach has gained increasing traction, as it offers better flexibility and deployment potential in infrastructure-sparse areas, alongside demonstrably higher accuracy. This is evidenced by a reduction in localization error from under 300m (achieved by deploying over 70 static gateways [13]) to under 100m using just a single mobile sensor [1].

The received signal strength indicator (RSSI) has widely been adopted for the localization using a mobile sensor [19], [36]. For one thing, RSSI has long been considered suitable for localization in non-line-of-sight (NLOS) environments, in contrast to other signal modalities, such as angle of arrival (AoA), time of flight (ToF), and time difference of arrival (TDoA) [9], [14], [15], [36], [37]. For another, reading RSSI does not require specialized hardware, making it the easiest to obtain [1], [38]–[40].

Prior studies on LoRa tag localization using mobile sensors mainly employ RSSI ranging, heuristic search, or reinforcement learning (RL) [14], [41]. Ranging methods estimate the signal travel distance for localization [16], [20], [42], [43], but are often prone to large errors in practice due to inaccurate distance estimates. Heuristic methods craft rules to guide the sensor toward the tag [44], [45]. For instance, the Nelder-Mead simplex algorithm samples simplices on the heatmap to find higher RSSI, while the Robbins-Monro algorithm incorporates noise robustness [18], [19], [46]. Nevertheless, these methods typically rely on assumptions about the heatmap’s landscape—such as convexity, smoothness, or monotonicity—which limits their effectiveness given the complex and unpredictable nature of real-world RSSI distributions. Reinforcement learning (RL) has emerged as a promising approach that avoids such landscape assumptions, with various standard models applied to this problem [1], [22], [47]. However, existing RL methods are often designed for

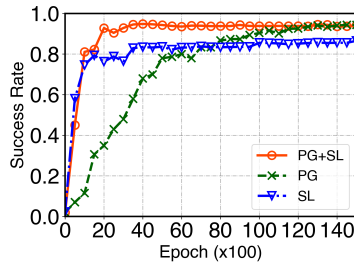


Fig. 20. Training efficiency study ($\omega_2 = 1$).

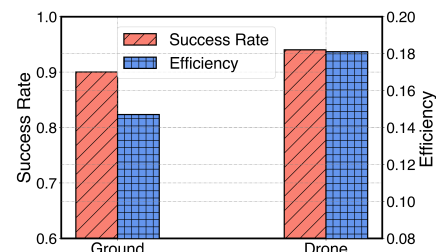


Fig. 21. Performance in ground and drone search.



Fig. 22. Case study: trajectory in ground search

and tested in a single, specific scenario. They do not fully account for domain shift and signal fluctuation in practical, general settings. Consequently, decision errors can propagate and compound throughout the search, leading to myopic behaviors like premature convergence, path divergence, or looping, often culminating in substantial localization errors and search inefficiencies.

To overcome this, we propose LoRaCompass, the first reinforcement learning model design to efficient LoRa tag search robust against signal fluctuation and domain shift. LoRaCompass proposes a robust representation from RSSI spatial feature to enable exploitation under domain shift and signal fluctuation, via a spatially-aware feature extractor and a policy distillation loss function. It also introduces the first exploration function that accounts for uncertainty in LoRa tag search. Altogether, LoRaCompass allows the mobile sensor to sequentially move toward a LoRa tag with increasing confidence, notwithstanding domain shift and signal fluctuation.

VI. CONCLUSION

We study the sequential-decision making process for a mobile LoRa sensor to locate a LoRa tag using the received signal strength indicator (RSSI) at the sensor, which is fundamental to the tracking of mentally incapacitated patients (MIPs) and others that may go missing. This search process is challenging in a general, unknown environment due to domain shift and signal fluctuation, as the mobile sensor needs to navigate an unknown, largely non-convex, and noise-contaminated RSSI landscape. This hurdles previous works from an accurate and efficient tag localization.

We introduced LoRaCompass, a novel reinforcement-learning model to efficiently search for LoRa tag under domain shift and signal fluctuation. By tailoring exploitation and exploration to this problem, LoRaCompass can navigate the mobile sensor hopping toward the tag with increasing confidence. For robust exploitation, LoRaCompass captures from the RSSI spatial variation a robust representation for moving direction under domain shift and signal fluctuation, via a novel feature extractor and a policy distillation loss function. It then introduces a closed-form exploration function inspired by upper confidence bound (UCB) to proactively reduces decision uncertainty. Through extensive experiments and system deployments in both ground-based and drone-assisted scenarios in diverse, unseen environments of more than 80km^2 , LoRaCompass achieves an impressive success

rate of over 90%, outperforming previous methods by 40%, with a satisfactory near-linear efficiency. Our future work will focus on extending LoRaCompass to multi-sensor settings, where collaborative efforts can enhance the search performance for LoRa tags, paving the way for more effective applications in search and rescue operations, location-based services, and AI healthcare.

REFERENCES

- [1] M. N. Soorki, H. Aghajari, S. Ahmadiinabi, H. B. Babadegani, C. Chacour, and W. Saad, "Catch me if you can: Deep meta-rl for search-and-rescue using lora uav networks," *IEEE Transactions on Mobile Computing*, vol. 24, pp. 763 – 778, 2025.
- [2] L. Aldhaheri, N. Alshehhi, I. I. J. Manzil, R. A. Khalil, S. Javaid, N. Saeed, and M.-S. Alouini, "LoRa communication for agriculture 4.0: Opportunities, challenges, and future directions," *IEEE Internet of Things Journal*, 2024.
- [3] C. O. Quero and J. Martinez-Carranza, "Unmanned aerial systems in search and rescue: A global perspective on current challenges and future applications," *International Journal of Disaster Risk Reduction*, vol. 118, no. 105199, p. 105199, 2025.
- [4] B.-B. Zhang, D. Zhang, R. Song, B. Wang, Y. Hu, and Y. Chen, "Rf-search: Searching unconscious victim in smoke scenes with rf-enabled drone," in *Proceedings of the 29th Annual International Conference on Mobile Computing and Networking*. Madrid, Spain: ACM, 2023, pp. 1–15.
- [5] K. Tong, Y. Hu, B. Dikic, S. Solmaz, F. Fraundorfer, and D. Watzenig, "Robots saving lives: A literature review about search and rescue (sar) in harsh environments," in *2024 IEEE Intelligent Vehicles Symposium (IV)*. Jeju Island, Korea: IEEE, 2024, pp. 953–960.
- [6] M. P. Manuel, M. Faied, and M. Krishnan, "A lora-based disaster management system for search and rescue mission," *IEEE Internet of Things Journal*, vol. 11, pp. 34 024–34 034, 2024.
- [7] Y. Hu, M. Chen, W. Saad, H. V. Poor, and S. Cui, "Distributed multi-agent meta learning for trajectory design in wireless drone networks," *IEEE Journal on Selected Areas in Communications*, vol. 39, no. 10, pp. 3177–3192, 2021.
- [8] X. Fan, G. Li, Z. Lin, Y. Hu, Y. Liu, T. Jiang, Z. Yin, F. Qian, S. Wang, and S.-H. G. Chan, "Experiences of deploying a citywide crowdsourcing platform to search for missing people with dementia," in *Proceedings of the 30th Annual International Conference on Mobile Computing and Networking*. D.C., USA: ACM, 2024, pp. 200–214.
- [9] T. He, J. Tan, W. Zhuo, M. Printz, and S.-H. G. Chan, "Tackling Multipath and Biased Training Data for IMU-Assisted BLE Proximity Detection," in *IEEE INFOCOM 2022-IEEE Conference on Computer Communications*. IEEE, 2022, pp. 1259–1268.
- [10] M. I. Hany, H. Rizk, and M. Youssef, "AirTags for Human Localization, Not Just Objects," in *Proceedings of the 2nd ACM SIGSPATIAL International Workshop on Geo-Privacy and Data Utility for Smart Societies*, 2024, pp. 13–18.
- [11] T. Hadwen, V. Smallbon, Q. Zhang, and M. D'Souza, "Energy Efficient LoRa GPS Tracker for Dementia Patients," in *2017 39th annual international conference of the IEEE engineering in medicine and biology society (EMBC)*. IEEE, 2017, pp. 771–774.

[12] P. Sadeghian, J. Håkansson, and X. Zhao, "Review and Evaluation of Methods in Transport Mode Detection based on GPS Tracking Data," *Journal of Traffic and Transportation Engineering*, vol. 8, no. 4, pp. 467–482, 2021.

[13] Y. Li, J. Barthelemy, S. Sun, P. Perez, and B. Moran, "Urban vehicle localization in public lorawan network," *IEEE Internet of Things Journal*, vol. 9, no. 12, pp. 10283–10294, 2021.

[14] Z. Shi, C. Gu, S. He, and K. Hu, "Enable angle of arrival in lora for efficient indoor localization," in *LoRa Localization: System Design and Performance Analysis*. Switzerland: Springer, 2024, pp. 59–74.

[15] S. Elsherif, K. Tarek, P. Edward, and T. Elshabrawy, "Theoretical and practical evaluation of lora-based ranging towards accurate tdoa-based lora localization," *IEEE Communications Letters*, vol. 7, pp. 923–927, 2025.

[16] F. B. Sorbelli, C. M. Pinotti, S. Silvestri, and S. K. Das, "Measurement errors in range-based localization algorithms for uavs: Analysis and experimentation," *IEEE Transactions on Mobile Computing*, vol. 21, no. 4, pp. 1291–1304, 2020.

[17] S. Shen, Z. Ma, M. Liu, Q. Liu, Y. Bai, and M. Xiong, "A cloud-terminal collaborative system for crowd counting and localization using multi-uavs," in *IEEE INFOCOM 2022-IEEE Conference on Computer Communications Workshops (INFOCOM WKSHPS)*. New York, NY, USA: IEEE, 2022, pp. 1–6.

[18] P. Toulis, T. Horel, and E. M. Airoldi, "The proximal robbins-monro method," *Journal of the Royal Statistical Society Series B: Statistical Methodology*, vol. 83, no. 1, pp. 188–212, 2021.

[19] F. Gao and L. Han, "Implementing the nelder-mead simplex algorithm with adaptive parameters," *Computational Optimization and Applications*, vol. 51, no. 1, pp. 259–277, 2012.

[20] Z. Zhu, J. He, L. Hou, L. Xu, W. Zhu, and L. Wang, "Emergency localization for mobile ground users: An adaptive uav trajectory planning method," in *IEEE INFOCOM 2024-IEEE Conference on Computer Communications Workshops (INFOCOM WKSHPS)*. Vancouver, BC, Canada: IEEE, 2024, pp. 1–6.

[21] R. Kirk, A. Zhang, E. Grefenstette, and T. Rocktäschel, "A survey of zero-shot generalisation in deep reinforcement learning," *Journal of Artificial Intelligence Research*, vol. 76, pp. 201–264, 2023.

[22] E. Ossongo, M. Esseghir, and L. Merghem-Boulahia, "A multi-agent federated reinforcement learning-based optimization of quality of service in various lora network slices," *Computer Communications*, vol. 213, pp. 320–330, 2024.

[23] J. Moos, K. Hansel, H. Abdulsamad, S. Stark, D. Clever, and J. Peters, "Robust Reinforcement Learning: A Review of Foundations and Recent Advances," *Machine Learning and Knowledge Extraction*, vol. 4, no. 1, pp. 276–315, 2022.

[24] Y. Wang and S. Zou, "Online Robust Reinforcement Learning with Model Uncertainty," *Advances in Neural Information Processing Systems*, vol. 34, pp. 7193–7206, 2021.

[25] P. Auer, N. Cesa-Bianchi, and P. Fischer, "Finite-time Analysis of the Multiarmed Bandit Problem," *Machine learning*, vol. 47, no. 2, pp. 235–256, 2002.

[26] C. Tang, B. AbbateMatteo, J. Hu, R. Chandra, R. Martín-Martín, and P. Stone, "Deep reinforcement learning for robotics: A survey of real-world successes," in *Proceedings of the AAAI Conference on Artificial Intelligence*, vol. 39. Philadelphia, Pennsylvania, USA: AAAI, 2025, pp. 28694–28698.

[27] M. Aernouts, R. Berkvens, K. Van Vlaenderen, and M. Weyn, "Sigfox and lorawan datasets for fingerprint localization in large urban and rural areas," *Data*, vol. 3, no. 2, p. 13, 2018.

[28] D. Guo, C. Gu, L. Jiang, W. Luo, and R. Tan, "Illoc: In-hall localization with standard lorawan uplink frames," *Proceedings of the ACM on Interactive, Mobile, Wearable and Ubiquitous Technologies*, vol. 6, no. 1, pp. 1–26, 2022.

[29] Y. Jiang, J. Z. Kolter, and R. Raileanu, "Uncertainty-driven exploration for generalization in reinforcement learning," in *Deep Reinforcement Learning Workshop NeurIPS 2022*. Mexico City: NIPS, 2022.

[30] J. Guo, C. P. Chen, Z. Liu, and X. Yang, "Dynamic neural network structure: A review for its theories and applications," *IEEE Transactions on Neural Networks and Learning Systems*, vol. 36, no. 3, pp. 4246–4266, 2024.

[31] X. Zhao, L. Wang, Y. Zhang, X. Han, M. Deveci, and M. Parmar, "A review of convolutional neural networks in computer vision," *Artificial Intelligence Review*, vol. 57, no. 4, p. 99, 2024.

[32] X. Wang, S. Wang, X. Liang, D. Zhao, J. Huang, X. Xu, B. Dai, and Q. Miao, "Deep reinforcement learning: A survey," *IEEE Transactions on Neural Networks and Learning Systems*, vol. 35, no. 4, pp. 5064–5078, 2022.

[33] L. Fan, G. Wang, D.-A. Huang, Z. Yu, L. Fei-Fei, Y. Zhu, and A. Anandkumar, "Secant: Self-expert cloning for zero-shot generalization of visual policies," in *ICML 2021*. Online: ICML, 06 2021, p. 16.

[34] N. Le, V. S. Rathour, K. Yamazaki, K. Luu, and M. Savvides, "Deep reinforcement learning in computer vision: A comprehensive survey," *Artificial Intelligence Review*, vol. 55, no. 4, pp. 2733–2819, 2022.

[35] P. Ladosz, L. Weng, M. Kim, and H. Oh, "Exploration in deep reinforcement learning: A survey," *Information Fusion*, vol. 85, pp. 1–22, 2022.

[36] L. E. Marquez and M. Calle, "Understanding lora-based localization: Foundations and challenges," *IEEE Internet of Things Journal*, vol. 10, no. 13, pp. 11185–11198, 2023.

[37] B. Yuan, R. He, B. Ai, R. Chen, G. Wang, J. Ding, and Z. Zhong, "A uav-assisted search and localization strategy in non-line-of-sight scenarios," *IEEE Internet of Things Journal*, vol. 9, no. 23, pp. 23841–23851, 2022.

[38] E. H. Yoshitome, J. V. R. da Cruz, M. E. P. Monteiro, and J. L. Rebelatto, "Lora-aided outdoor localization system: Rssi or tdoa?" *Internet Technology Letters*, vol. 5, no. 2, p. e319, 2022.

[39] X. Wang, L. T. Yang, D. Meng, M. Dong, K. Ota, and H. Wang, "Multi-uav cooperative localization for marine targets based on weighted subspace fitting in sagin environment," *IEEE Internet of Things Journal*, vol. 9, no. 8, pp. 5708–5718, 2021.

[40] Y. Teng, P. Zhang, S. Zhao, X. Jiang, Y. Shen, and F. Xiao, "Secure device authentication for mmwave mimo systems via mutual coupling and spatial aoa," in *IEEE INFOCOM 2025-IEEE Conference on Computer Communications*. London, UK: IEEE, 2025, pp. 1–10.

[41] H. Ruan, P. Sun, Y. Dong, H. Tahaei, and Z. Fang, "An overview of lora localization technologies," *Computers, Materials & Continua*, vol. 82, no. 2, pp. 1645–1680, 2025.

[42] Y. Bakhuraisa, H. S. Lim, Y. K. Chan, and M. Hilman, "Uav-assisted localization of ground nodes in urban environments using path loss measurements," *Drones*, vol. 9, no. 6, p. 450, 2025.

[43] G. M. Bianco, R. Giuliano, G. Marrocco, F. Mazzenga, and A. Mejia-Aguilar, "Lora system for search and rescue: Path-loss models and procedures in mountain scenarios," *IEEE Internet of Things Journal*, vol. 8, no. 3, pp. 1985–1999, 2020.

[44] J. Larson, M. Menickelly, and S. M. Wild, "Derivative-free optimization methods," *Acta Numerica*, vol. 28, pp. 287–404, 2019.

[45] V. Mikhalevich, A. Gupal, and V. Norkin, "Methods of nonconvex optimization," *arXiv preprint arXiv:2406.10406*, 2024.

[46] M. Selvam, M. Ramachandran, and V. Saravanan, "Nelder–mead simplex search method-a study," *Data Analytics and Artificial Intelligence*, vol. 2, no. 2, pp. 117–122, 2022.

[47] D. Ebrahimi, S. Sharafeddine, P.-H. Ho, and C. Assi, "Autonomous uav trajectory for localizing ground objects: A reinforcement learning approach," *IEEE Transactions on Mobile Computing*, vol. 20, no. 4, pp. 1312–1324, 2020.

[48] J. Fan, B. Jiang, and Q. Sun, "Hoeffding's inequality for general markov chains and its applications to statistical learning," *Journal of Machine Learning Research*, vol. 22, no. 139, pp. 1–35, 2021.

APPENDIX

VISUALIZATION OF RSSI HEATMAP

Figure 23 illustrates the RSSI heatmaps of the five sites of $4.1 \times 4.1 \text{ km}^2$ used in our experiment. The first three rows present the different snapshot of the same site at different time; the last row shows the underlying heatmap of RSSI expectation (approximated by the mean of massive samples). These heatmaps clearly reveal significant domain shift and signal fluctuation, due to various environmental factors such as buildings, vegetation, terrain, and dynamic factors like multipath fading, moving objects, and ambient noise. While the RSSI are noisy on a local scale, they show a clear, robust pattern from a global, macro perspective. This provides a robust representation of action for a search agent to hop to the tag proximity.

DERIVATION OF EXPLORATION FUNCTION

The exploration function $g(a, \mathcal{M}_k)$ is defined in Eq. (22), and the objective of action execution is defined in Eq. (21). In

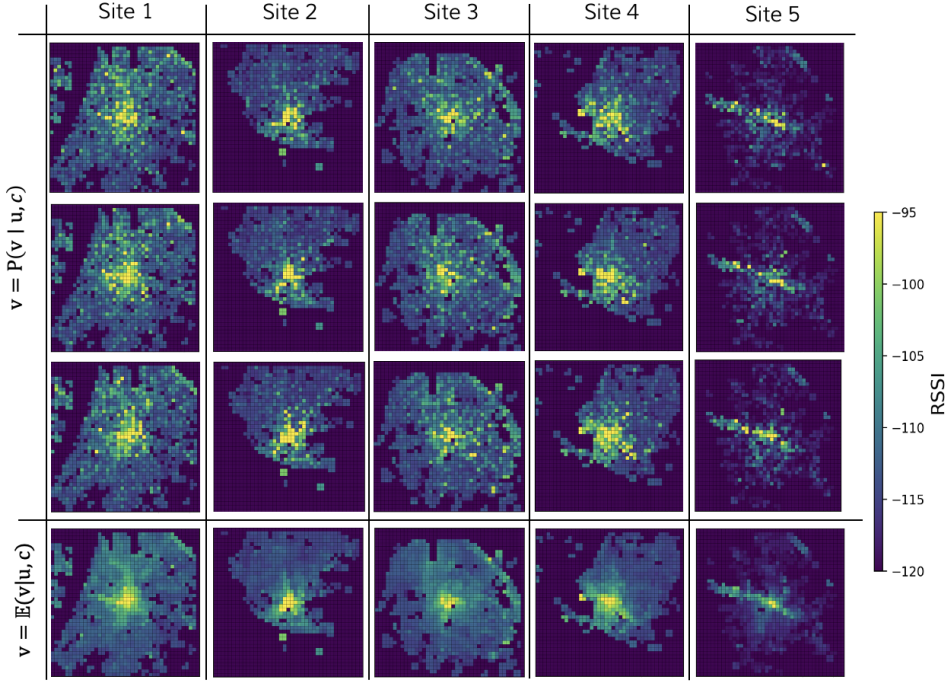


Fig. 23. Illustration of RSSI heatmaps in $4.1 \times 4.1 \text{ km}^2$. Recall that an RSSI observation v is sampled from the observation function $P(v | u, c)$, depending on the agent location u and tag location c (from Eq. (2)).

this section, we show that $g(a, \mathcal{M}_k)$ can be used to achieve the objective of the action execution, expressed as

$$\begin{aligned} & \arg \max_{a_k \in \mathcal{A}} \left[\pi_e(a_k | \mathcal{M}_k) - \beta_k |\pi_e(a_{k+1} | \mathcal{M}_{n+1}) \right. \\ & \quad \left. - \pi_e(a_{k+1} | \mathbb{E}(\mathcal{M}_{k+1})) \right] \quad (26) \\ & \approx \arg \max_{a_k \in \mathcal{A}} [\pi_e(a_k | \theta) + g(a_k, \mathcal{M}_k)]. \end{aligned}$$

First, we provide a detailed explanation of the uncertainty term in Eq. (26). The probability estimate of the exploitation model at step $k+1$ is $\pi_e(a_{k+1} | \mathcal{M}_{k+1})$. The uncertainty in the estimation stems from aleatoric uncertainty and epistemic uncertainty. Here, we discuss uncertainty from the perspective of the whole decision-making sequence. The aleatoric uncertainty refers to the uncertainty in the mapping from a fully-visible feature map to an action, i.e., $\mathbb{E}(\mathcal{M}_{k+1}) \mapsto a_{k+1}$. On the other hand, the epistemic uncertainty is the discrepancy of the probability distribution of actions predicted from a given feature map and its fully-visible counterpart, shown as

$$|\pi_e(a_{k+1} | \mathcal{M}_{k+1}) - \pi_e(a_{k+1} | \mathbb{E}(\mathcal{M}_{k+1}))|, \quad (27)$$

where the calculation of $|\cdot|$ follows Eq. (20). Our context fulfills the three conditions in which aleatoric uncertainty is negligible: (1) the receptive field (or feature map size) is sufficiently large; (2) the action space (\mathcal{A}) is limited; (3) the exploitation model (based on deep learning) has sufficient learning capacity. Based on the conditions above, the decision uncertainty can be regarded as the epistemic uncertainty in Eq. (27).

Given the same model parameter θ , the epistemic uncertainty depends on the feature map \mathcal{M}_{k+1} . Since we can

derive other two maps using signal map, we use feature map discrepancy to estimate the uncertainty, shown as

$$\begin{aligned} & |\pi_e(a_{k+1} | \mathcal{M}_{k+1}) - \pi_e(a_{k+1} | \mathbb{E}(\mathcal{M}_{k+1}))| \\ & \approx \gamma_1 |\mathcal{M}_{k+1} - \mathbb{E}(\mathcal{M}_{k+1})| \\ & = \gamma_2 \gamma_1 \left| \mathcal{M}_{k+1}^{(s)} - \mathbb{E}(\mathcal{M}_{k+1}^{(s)}) \right| \\ & = \gamma_2 \gamma_1 \sum_{\bar{v} \in \mathcal{M}_{k+1}^{(s)}} |\bar{v} - \mathbb{E}(v)|. \end{aligned} \quad (28)$$

Here, $\mathbb{E}(\mathcal{M}_{k+1}^{(s)}) = \{\mathbb{E}(v)\}$ is the fully-visible signal map, and $\gamma_1, \gamma_2 \in \mathbb{R}$ are two constants (note that $\mathbb{E}(v) = \mathbb{E}(\bar{v})$).

We cannot directly measure \bar{v} and $\mathbb{E}(v)$ in Eq. (28). Inspired by Upper Confidence Bound (UCB), we use Hoeffding's inequality [48] to estimate the *upper bound* of their difference $\epsilon(u)$, shown as

$$\begin{aligned} & P(|\bar{v}(u) - \mathbb{E}(v(u))| \geq \epsilon(u)) \\ & \leq 2 \exp \left(-\frac{2n(u)\epsilon^2(u)}{(v_{max} - v_{min})^2} \right), \end{aligned} \quad (29)$$

where $n(u)$ is the number of visits at u , and v_{max}, v_{min} are the extremum values of RSSI (in our case, $v_{max} = -30, v_{min} = -120$). With a confidence level $\sigma \in [0, 1]$, the upper bound depends on the visit number, shown as

$$\begin{aligned} \epsilon(u) &= (v_{max} - v_{min}) \sqrt{\frac{-\log(\sigma/2)}{2n(u)}} \\ &= \gamma_3 \sqrt{\frac{-\log(\sigma/2)}{n(u)}}, \end{aligned} \quad (30)$$

where $\gamma_3 \in \mathbb{R}$ is a constant. If we apply Eq. (30) to Eq. (28), the computation needs to traverse the whole signal map (or, it

requires additional memory). Since $\mathcal{M}_{k+1}^{(s)}$ differentiates from $\mathcal{M}_k^{(s)}$ only by a_{k+1} , rather than estimating Eq. (28), a more *lightweight* practice is to estimate the uncertainty reduction due to an action, given as

$$\begin{aligned} & \arg \max_{a_k \in \mathcal{A}} \left[\pi_e(a_k \mid \mathcal{M}_k) - \beta_k \left| \pi_e(a_{k+1} \mid \mathcal{M}_{k+1}) \right. \right. \\ & \quad \left. \left. - \pi_e(a_{k+1} \mid \mathbb{E}(\mathcal{M}_{k+1})) \right| \right] \\ & \approx \arg \max_{a_k \in \mathcal{A}} \left[\pi_e(a_k \mid \mathcal{M}_k) \right. \\ & \quad \left. + \beta_k \left(\left| \pi_e(a_k \mid \mathcal{M}_k) - \pi_e(a_k \mid \mathbb{E}(\mathcal{M}_k)) \right| \right. \right. \\ & \quad \left. \left. - \left| \pi_e(a_{k+1} \mid \mathcal{M}_{k+1}) - \pi_e(a_{k+1} \mid \mathbb{E}(\mathcal{M}_{k+1})) \right| \right) \right], \end{aligned} \quad (31)$$

where the approximation is based on a sufficiently large receptive field. Applying Eq. (30) to Eq. (31), we have

$$\begin{aligned} & \left| \pi_e(a_k \mid \mathcal{M}_k) - \pi_e(a_k \mid \mathbb{E}(\mathcal{M}_k)) \right| \\ & - \left| \pi_e(a_{k+1} \mid \mathcal{M}_{k+1}, \theta) - \pi_e(a_{k+1} \mid \mathbb{E}(\mathcal{M}_{k+1})) \right| \\ & \approx \gamma_2 \gamma_1 \left(\sum_{\bar{v} \in \mathcal{M}_n^{(s)}} |\bar{v} - \mathbb{E}(v)| - \sum_{\bar{v} \in \mathcal{M}_{n+1}^{(s)}} |\bar{v} - \mathbb{E}(v)| \right) \quad (32) \\ & \approx \gamma_3 \gamma_2 \gamma_1 \sqrt{-\log(\sigma/2)} \left(\frac{1}{\sqrt{n_a}} - \frac{1}{\sqrt{n_a + 1}} \right), \end{aligned}$$

where $n_a = n(u_{k+1} \mid u_k, a) + 1$ is the visit count of the agent location at step $k + 1$ if action a is executed (here, we adjust the denominator to avoid the issue of division by zero).

Based on this estimation, we tune the confidence level σ based on Δv_k from Eq. (23), which is the gap between the current RSSI observation v_k and the reference $\bar{v}(c)$. Intuitively, the smaller the gap, the higher probability that the tag is in the proximity to the agent, and we use the *Sigmoid function* to model their relationship. Therefore, we model the confidence level as a function of the RSSI gap Δv , shown as

$$\sigma(\Delta v) = 2 \exp \left[-\gamma_4 \left(\text{Sigmoid}(\alpha \Delta v) - \frac{1}{2} \right)^2 \right], \quad (33)$$

where $\gamma_4 \in \mathbb{R}$ is a constant, and $\alpha \in \mathbb{R}$ is the proximity parameter. By applying Eq. (33) to Eq. (32), we have the exploration function in Eq. (22) to achieve the objective in Eq. (21), where the variable $\beta = \gamma_1 \gamma_2 \sqrt{\gamma_4}$.